Soil & Tillage Research 260 (2026) 107139

Contents lists available at ScienceDirect

Soil & Tillage Research

journal homepage: www.elsevier.com/locate/still

Dynamics and consequences of compaction process in agricultural soil under vehicular loading – High-sampling-rate measurements and structural analyses

Sampo Kulju [a,*], Harri Lindeman [a], Mika Tähtikarhu [b], Johanna Nikama [c], Jukka Kuva [d], Jari Ala-Ilomäki [b], Jari Hyväluoma [c]

[a] Natural Resources Institute Finland (Luke), Tekniikankatu 1, Tampere 33720, Finland
[b] Natural Resources Institute Finland (Luke), Latokartanonkaari 9, Helsinki 00790, Finland
[c] Natural Resources Institute Finland (Luke), Tietotie 4, Jokioinen 31600, Finland
[d] Geological Survey of Finland, Vuorimiehentie 2K, Espoo 02150, Finland

ARTICLE INFO

Keywords:
Soil compaction
Bolling probe
Pressure
Volumetric water content
High-sampling-rate
X-ray tomography

ABSTRACT

Soil compaction induced by vehicle traffic on agricultural fields threatens soil health. Thus, stress caused by heavy machinery, and its effects on soil, have been widely studied by experimental and computational methods. This study presents a high-sampling-rate Bolling probe setup for dynamic soil stress measurements and a continuous Percometer measuring system to investigate the effect of a vehicular load on soil moisture. Both systems were implemented in a field test area where ten passes with an agricultural tractor were driven on a test track. The on-site measurements were accompanied by laboratory analysis of soil structure and strength analyses based on soil samples taken from the field test site before and after the vehicle passes. In addition to ten compaction passes, a high-speed vehicle pass was performed to test the capabilities of our experimental setup. Results of the Bolling probe and Percometer measurements showed new aspects on the dynamics of soil stress and the state of soil moisture caused by a vehicular loading. Measured stress and soil moisture values also indicated that soil was compacting due to vehicle passes, an effect which was confirmed by X-ray tomography imaging and laboratory analyses of soil samples. During the high-speed pass, our Bolling probe setup was able to measure oscillations of soil stress.

1. Introduction

Soil compaction is a severe and long-lasting threat to soil functioning (Keller et al., 2021) and an increasing risk in modern agriculture, where a trend is towards more powerful and at the same time heavier machines and implements (Keller et al., 2019). Water content is an essential component of a soil compaction process. An increase in water content causes a decrease to the load bearing capacity of soil (Hamza and Anderson, 2005). Thereby, compaction increases due to field traffic on wet soils (Alakukku et al., 2003) and compaction risks further increase in predicted more extreme weather patterns in the future climate.

A considerable fraction of arable land is considered to suffer from compaction (e.g. Brus and van den Akker, 2018). Soil compaction has been considered mostly to threaten subsoil, where the recovery times are very slow, decades or even centuries (Schjønning et al., 2015). While tillage operations loosen the soil, they do not undo all the compaction effects which have been found to persist even in ploughed topsoil for several years (Arvidsson and Håkansson, 1996). Soil compaction adversely affects many important functions and ecosystem services provided by soils including soil hydraulic properties, nutrient cycling, and soil biodiversity. Compaction can reduce water infiltration and storage as well as aeration and soil respiration and increase the probability of anoxic conditions. All these can result in harmful effects such as increased surface runoff and thereby soil erosion, losses of nutrients and gaseous emissions of greenhouse gases (Nawaz et al., 2013, Cambi et al., 2015).

Soil compaction caused by field traffic and soil stress induced by vehicles has been studied experimentally and modeled according to pressure data measured by Bolling probes (Keller and Lamandé 2010, Keller et al., 2016). However, sampling frequencies of Bolling probe and

* Corresponding author.
E-mail address: sampo.kulju@luke.fi (S. Kulju).

https://doi.org/10.1016/j.still.2026.107139
Received 14 May 2025; Received in revised form 3 February 2026; Accepted 16 February 2026
Available online 19 February 2026

load cell measurements have been relatively low, in the range of tens of Hz (Schäffer et al., 2007, Berisso et al., 2013), which have been limiting driving speeds during experiments. In addition, a low sampling rate may result in loss of process information, because of a large time step between measured data points. Thus, loading-induced dynamic phenomena in soil, associated with higher vehicle speeds, would be hard or even impossible to observe.

Research articles about the effects of loading on the mechanical properties of soil cover a wide time spectrum, from instant consequences (Chen et al., 2019; Ghadernejad et al., 2018; Shahgholi and Abuali, 2015) to long-term impacts (DeArmond et al., 2019). The effects of vehicular loading on hydraulic and structural parameters of soil have also been investigated in time frames concerning a vehicular pass (Yadav et al., 2020). However, the high-frequency behavior and dynamics of soil moisture during a loading from a moving vehicle have not been thoroughly investigated.

In this article we present a set of methods to investigate soil compaction process with high-sampling-rate measurements of soil pressure and moisture profiles. The high-sampling-rate measurements were complemented with soil physical analyses that provided supplementary information about the changes in soil structure due to vehicular loading.

2. Methods

The focus of this work was to test and demonstrate the capabilities of our high-sampling-rate Bolling probe and Percometer instrumentations. Thus, drive tests consisting of multiple vehicle passes on an instrumented test track were performed. In addition, to get the full picture of soil properties of the test track, soil samples were taken from the test area before and after vehicle passes. Soil samples were used for water retention and soil strength analyses and for X-ray tomography imaging. The collected datasets were analyzed with various methods, such as signal processing, image analysis and statistical methods. Detailed descriptions of all the methods are presented in the following sections.

2.1. Field test setup

For the drive test, a straight 25 m long and 5 m wide instrumented test track was laid out (Fig. 1). A total of eleven passes were driven on the track, where the 11th pass was driven at elevated speed. The number of passes was determined on the basis of our previous studies on soil compaction showing that the largest increase in soil density occurs during the first passes and the state of compaction essentially stabilizes during ten passes (Toivio et al., 2017). To aid a tractor driver and to assure the constant travel path of the tractor wheels, an intended wheel travel line was marked on the test track with spray paint. A total of 36 penetration resistance and rut depth measurement points were marked at intended paths of wheel travel with spray paint at two 5 m long sections before and after the instrumented section (Fig. 1). The designated instrumented and measuring sections of the test track started with the penetrometer and rut depth measurement section, followed by the Bolling probe and Percometer measurement section. The test track was finalized by two soil sample sections. Each section was 5 m in length.

All measurements were performed before the test drives, after the 2nd pass, and 10th pass to measure the effect of the first passes and the stabilized state as the number of passes increased. Soil pressure (Fig. 1: BP) and soil moisture (PM) were measured during the test drives. For soil pressure and soil moisture transducers, true depth (D), offset from tyre track centerline (O) and location along the test track (L) were measured after the test drives in conjunction with sensor removal.

Drive tests were performed with a four-wheel drive Valmet 705 agricultural tractor. The front axle weight of the tractor was 20.0 kN and the rear axle weight 22.6 kN. The tractor was equipped with 13.6 R 24 front tyres and 16.9 R 34 rear tyres and the tyre inflation pressure was 1.2 bar and 1.1 bar, respectively.

Soil samples for X-ray tomography, water retention measurements (Section A in Fig. 1a) and soil strength analysis (Section B in Fig. 1a) were taken from the test track at the wheel tracks before the drive experiment and after the 2nd and 10th test drives. For X-ray tomography, intact soil cores were sampled to aluminum cylinders with an inner diameter of 46 mm and a height of 70 mm. For water retention measurements, the sample diameter was 72 mm and height 48 mm, and for strength samples the diameter was 100 mm and height 30 mm. All soil

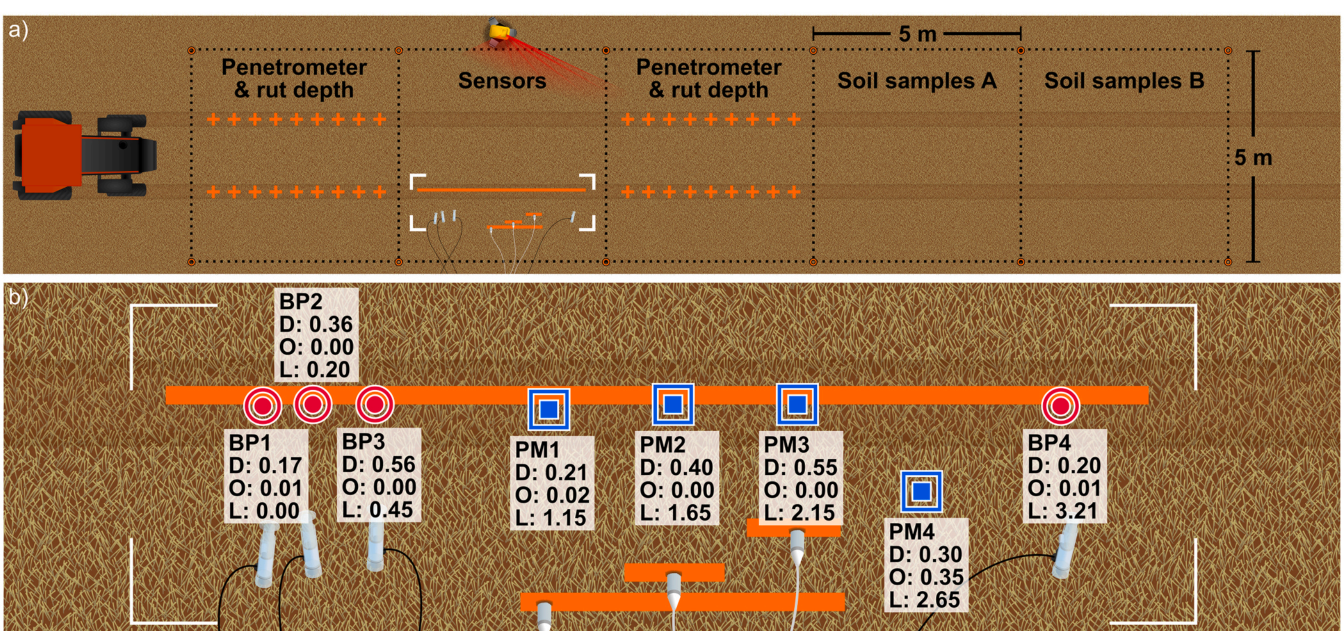

Fig. 1. Schematic figure of the experimental setup, subfigure a) presents sections which were designated for different methods and subfigure b) shows the close up of a sensor area with positions and coordinates of each Bolling probe (BP) and Percometer (PM). Coordinates are depth (D), offset (O) from the travel line and length (L) along the travel line direction measured from the position of BP1. The unit of the coordinates is m.

samples were taken below the depth of 2 cm. Five replicates were collected for each case. The collected soil samples were stored in their natural soil moisture at + 5 °C before laboratory analyses.

The experiment was carried out in autumn 2023. The study site is in southern Finland in Jokioinen (WGS84: 60.854° N, 23.462° E). The predominant soil type in the region is clay soil, but in the study site the topsoil is coarse textured and the subsoil is clayey (Geological Survey of Finland, 2015). The site has been under agricultural production and considering the five-year period before the experiment, the site was in cereal production except for the study year when pea was cultivated. The site had been tilled annually by autumn moldboard ploughing. The experiment was conducted after the harvest and before autumn tillage.

The soil at the study site was a loamy sand with clay, silt and sand contents of 6.3 %, 9.4 %, and 84.3 %, respectively. The textural classification was < 2 µm for clay, 2–63 µm for silt and 63 µm to 2 mm for sand. The carbon content of the soil was 2.1 %. Soil texture was analyzed from a composite soil sample collected from the topsoil of the study site from a depth of 0–15 cm. The soil was air-dried, ground and passed through a 2-mm sieve. The mass fractions of sand, silt and clay were determined by the pipette method described by Elonen (1971). Sieved samples were also analysed for the total carbon content with a Leco TruMac CN analyser (Leco Corporation, Michigan, USA).

2.2. Field test instrumentation

Changes in soil moisture during tractor passes were measured with four Percometer Dielectric Constant and Conductivity Meters by ADEK LLC (Fig. 2). Percometer (PM in Fig. 1b) is a 30 mm diameter tube probe measuring the dielectric constant, conductivity, and temperature of the soil. The antenna part of the probe is located along the 10 cm tip of the probe. The calculus of soil volumetric moisture is presented in Topp et al. (1980). The high-speed mode of the device enables measurements to be made at the rate of approximately 70 Hz as opposed to the measuring frequency of approximately 1 Hz of other sensors known to the authors. On the wheel track, the Percometers were aimed at the depths of 0.2 m, 0.4 m, and 0.6 m. The fourth Percometer was aimed 0.3 m off the wheel track outside the test track at a depth of 0.2 m. The goal of sensor placement was to capture moisture changes in relation to soil depth and distance outside the wheel track.

The effect of tractor wheel passes on soil pressure was measured with the Bolling probe (Keller et al., 2016). The Bolling probe (BP in Fig. 1b) consists of a rigid plastic tube with a pressure-sensing silicone hose tip of approximately 10 cm in length at the soil end, and a pressure transducer attached to the tube above the ground. The tube setup was inserted into a pre-drilled hole. The silicone tubes were aimed at the depths of 0.2 m, 0.4 m and 0.6 m, the last Bolling probe used for determining the forward speed of the tractor aimed at 0.2 m. The hose, tube, and sensor assembly was filled with water and a syringe above the ground was used to apply a pre-pressure to make the silicone hose to contact the pre-drilled hole in the soil. Hence, the changes in soil pressure could be observed above ground. To enable normal agricultural vehicle operating velocity in test drives, a high-speed soil pressure measuring hardware was set up. The pressure in the tubes was measured at a frequency of 2000 Hz with analogue Honeywell MIP –series pressure transducers and an MC LGR-5329 datalogger, capable of measuring frequency up to 200 kHz. The sampling rate of 2000 Hz is not especially high as such but is considerably higher than in previous studies with Bolling probes and load cells (Schäffer et al., 2007, Berisso et al., 2013).

Rut depth levels were measured with a self-leveling laser device. The system consists of a base unit sending a level laser beam rotating at 360°. The beam is detected with a receiver, the height position of which is recorded against a measuring rod resting on the deepest part of the wheel rut. Ground reference levels at rut depth points were measured before the test drives.

Soil penetration resistance was measured with an Eijkelkamp Penetrologger penetrometer. The device was pressed against the soil manually. Its display assisted the user in obtaining a steady penetration speed of 2 cm/s, and the penetration depth and resistance were measured electronically. A 60-degree cone of 1 cm^2 base area was used. Penetration resistance was measured at 0 cm to 80 cm depth.

2.3. Determination of soil physical properties

For the determination of soil mechanical properties, internal angle of friction ϕ and cohesion C, the soil samples were measured with Eijkelkamp 08.68 shear test apparatus. The shear tests were performed with normal pressure values of 50, 75, 100, 125, 150 and 175 kPa at a shear rate of 2 mm/min. The applied normal pressure falls in the range typical of nominal ground pressure of agricultural machinery. Due to failed tests, a full series of normal pressure values was not obtained for all soil samples. Sintered plates were placed on both sides of the sample to allow water to escape.

The soil moisture characteristic curves were determined using 100 kPa, 300 kPa and 500 kPa ceramic plates in pressure extractors (Soilmoisture Equipment Corp., Goleta, USA). The samples were first saturated for 14 days. The soil moisture characteristic curves were determined as drying curves by weighing the samples after equilibration in the following predefined suctions: 0.10, 0.25, 1.0, 3.1, 10, 100, and 310 kPa. The equilibration times varied between 3 and 21 days depending on the suction value. To determine the sample volume accurately, vertical and horizontal shrinkage of samples were measured at each suction with a Vernier caliper and a feeler gauge, respectively. The moisture content of soil samples was calculated as a quotient of the water volume in the sample by the volume of the shrunken sample. In addition, the wilting point 1600 kPa was produced osmotically by vapour pressure equilibrium with saturated ammonium oxalate solution. To derive pore size distribution from water retention curves, the suction values were converted to equivalent pore diameter d by using

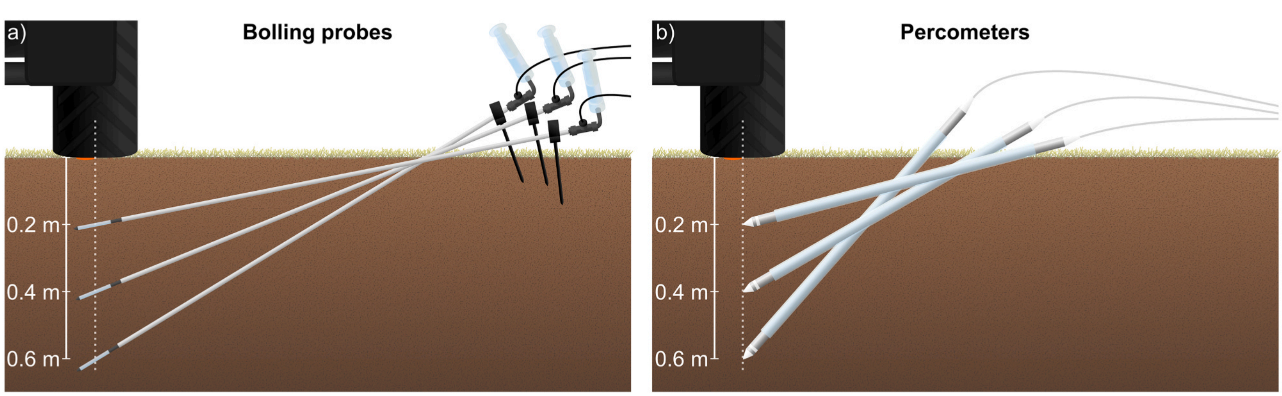

Fig. 2. Installation geometries of Bolling probes and Percometers for three different depths; 0.2, 0.4 and 0.6 m, under the travel line.

the Young-Laplace equation $d = 4\gamma/p$, where γ is the surface tension of water and p the suction pressure.

The X-ray tomography imaging was conducted with a GE phoenix v|tome|x s device (General Electric), administrated by the Geological Survey of Finland (GTK). Using the 240 kV microfocus tube with no beam filter, we used a tube current of 350 μA and an accelerating voltage of 100 kV, resulting in a power of 35 W. The number of projections was 2500 (full rotation of 360°, average over 3 exposures after waiting for a single exposure time at each angle). With a single exposure time of 250 ms, a single scan lasted a total of 42 min. The resulting 3D radiographs, reconstructed with phoenix datos|x software, had *a* voxel size of 30 μm (2024 ×2024 ×2024 voxels). They were converted to 16-bit grayscale image stacks for the quantitative image analyses using ThermoFisher PerGeos 2020.2.

2.4. Data analysis

2.4.1. Signal processing and analyzation of Bolling probe and Percometer data

Time series data collected from Bolling probes and Percometers were analyzed with scripts coded in Python programming language. Pressure sensors of Bolling probes are operating with a 5 V input voltage. The applied input voltage and the output voltage of each sensor were stored for each time step in mV by the datalogger. Voltage values from pressure sensors were converted to raw pressure values during the parsing of a data file by

$$p = \frac{4 \cdot (U_{out} - 0.1 \cdot U_{in}) \cdot 10^5}{0.8 \cdot U_{in}} \quad (1)$$

where p is pressure [Pa], U_{out} is an output voltage [mV] from a pressure sensor and U_{in} is the input voltage [mV] at the same time step. Also Percometers are measuring and storing voltage values in mV units. Conversion of these values to volumetric water content is explained later in this section. Examples of raw pressure data from Bolling probes and raw voltage data from Percometers are presented in Appendix A.

Bolling probes and Percometers measure pressure and voltage values from the test area even when there is no vehicular load on the sensors. In this article, these pressure and voltage levels before and after a vehicle pass are called base levels. A time frame consisting of a vehicular run over is called a dynamic compaction period. For visualizations and to ease the signal processing procedure, the raw data from Percometers were lowpass filtered to reduce noise. Lowpass filtering was performed with a Butterworth filter from the Python module Signal in the SciPy library. The critical frequency was set to 10.0 Hz. After lowpass filtering, the first and the last 5.0 s periods of time series from Percometer 1 for each vehicle pass were used to determine the range of a sensor output before and after the vehicle was run over the sensor area. These data ranges were used to search moments in time when vehicular load started and ended to affect the sensor output. Hereby, a dynamic compaction period could be automatically detected.

When the data period consisting of the run over was found, local extrema were searched from each half of this section. Thus, such time values where an axle of the tractor was on the sensor could be recorded. An example of lowpass filtered Percometer output and different signal points are presented in Fig. 3.

The moment where the front axle of the tractor was on Percometer 1 was set to be the origin (0.0 s) of Percometer data for each vehicle pass, and the time series from each sensor were shifted accordingly. A similar lowpass filtering and run-over-detection method was used for Bolling probe data, but the time series of Bolling probes were shifted by time values where the front axle was on Bolling probe 1.

After signal processing to search local extrema for both sensor types, the speed of the vehicle for each pass could be calculated. During the analysis of Percometer data, the speed was determined from a time interval between distinctive peaks in the Percometer 1 signal. With Bolling probes, a value for the speed was acquired by calculating it from the time interval between front axle peaks of Bolling probes 1 and 4, thus maximizing the traveled distance and used time, and in this way minimizing the error.

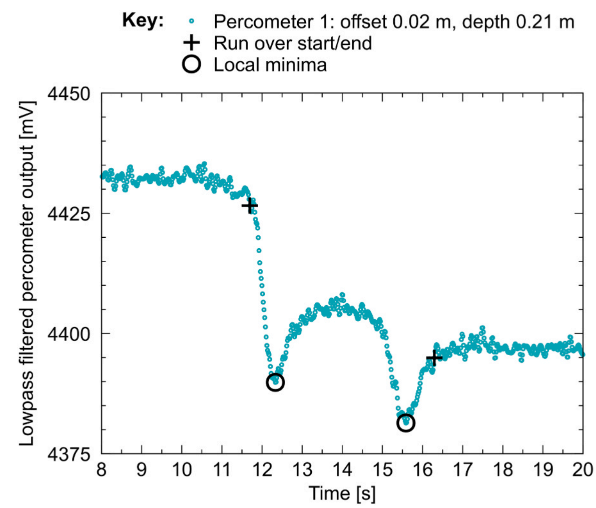

Fig. 3. Lowpass filtered data of the Percometer 1 (PM1) from vehicle pass one. The time frame of the vehicle passing over the sensor area was automatically detected. The start and end points are marked with crosses in the figure. From this time frame, the local minima were searched to pinpoint moments (marked with circles) when each axle of the vehicle was on the sensor.

Because of a human factor, the driving speed varied slightly between vehicle passes during the driving test. Thus, lowpass filtered and shifted time series from both sensor types were normalized by a scaling factor calculated from the speed of the vehicle. Time values were multiplied by the scaling factor

$$s_i = \frac{v_i}{v_1} \quad (2)$$

where v_i is the speed of the vehicle during the pass i and v_1 is the speed of the vehicle during the first pass.

Lowpass filtered, shifted and speed normalized Percometer values were used for the calculation of volumetric water content. Voltage values were converted to dielectric constant values ε_R by linear interpolation of calibration data. An example of a calibration curve is presented in Appendix B. Volumetric water content was calculated by an equation defined by Topp et al. (1980)

$$\theta_v = -5.3 \cdot 10^{-2} + 2.92 \cdot 10^{-2} \cdot \varepsilon_R - 5.5 \cdot 10^{-4} \cdot \varepsilon_R^2 + 4.3 \cdot 10^{-6} \cdot \varepsilon_R^3 \quad (3)$$

where ε_R is the dielectric constant.

2.4.2. Image analysis

To perform quantitative image analyses, the greyscale images resulting from X-ray tomography were converted to binary form. The greyscale values of the images were first calibrated, and the images were converted to 8-bit form using the greyscale values for the aluminum cylinder and air as reference densities (Larsbo et al., 2014; Turunen et al., 2019). A variance-weighted mean filter with a radius of 2 voxels was used to reduce noise from images (Gonzalez and Woods, 2008, Turpeinen, 2015). Segmentation of the images into solid and pore phases was done by manual thresholding. The same threshold value was applied for all images. Images were examined for sampling perturbations, and perturbed parts were excluded from the region of interest in subsequent image analyses.

Thresholded images were analyzed for porosity and pore size distribution. The total porosity visible in images with the used resolution was calculated from the segmented binary image by dividing the total number of pore voxels by the total number of voxels in the region of interest. Pore size distribution was obtained by successive application of a morphological opening operation (Horgan, 1998) with increasing diameter of the structuring element.

2.4.3. Rut depth and soil penetrating resistance

Rut depts were calculated by subtracting the ground reference level from the rut depth level. Average rut depths, after passes 2 and 10, were calculated from rut depths at 36 points. Medians of penetration resistance for 36 measurements were calculated for each depth from 0 to 80 cm before passes, after the 2nd and after the 10th pass. For penetration resistance measurements, the ground reference level was always used as zero, meaning that the measurement of the n^{th} pass started at the depth of the previously measured rut depth.

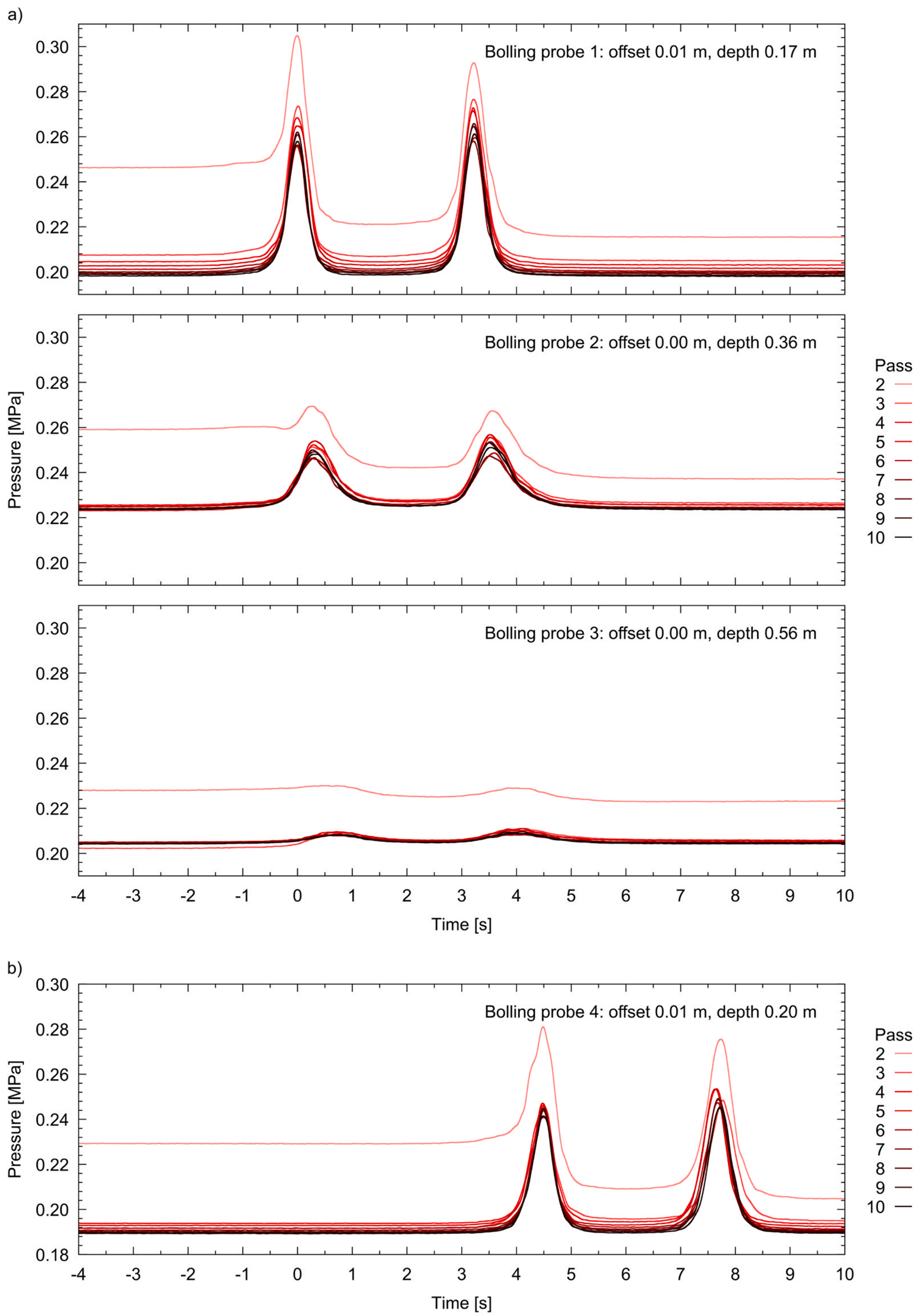

Fig. 4. Bolling probe values from vehicle passes two to ten. Data sets were lowpass filtered, zero seconds was set to be the moment when the front axle of the vehicle was on the Bolling probe 1 (BP1) and vehicle speed was normalized in relation to the first pass of the vehicle. Subfigure a) presents the three Bolling probes (1−3) at the start of the sensor area and subfigure b) is showing data from Bolling probe 4 (PM4) which was installed to the end of the sensor area to get data for the calculation of a vehicle speed. The offset from the travel line and the depth of each sensor are presented in subfigure labels.

2.4.4. Soil cohesion and the internal angle of friction from shear stress measurements

To determine cohesion and the internal angle of friction of soil, a linear function describing shear stress

$$\tau_i(\sigma) = C_i + \tan(\phi_i) \cdot \sigma \tag{4}$$

where τ_i is shear stress for pass i, C_i is cohesion, ϕ_i is an internal angle of friction and σ is normal stress applied to a sample, was fitted to experimental shear stress data sets.

2.4.5. Statistical analysis

One-way analysis of variance (ANOVA) was used to compare the soil physical properties and penetration resistance after varying numbers of

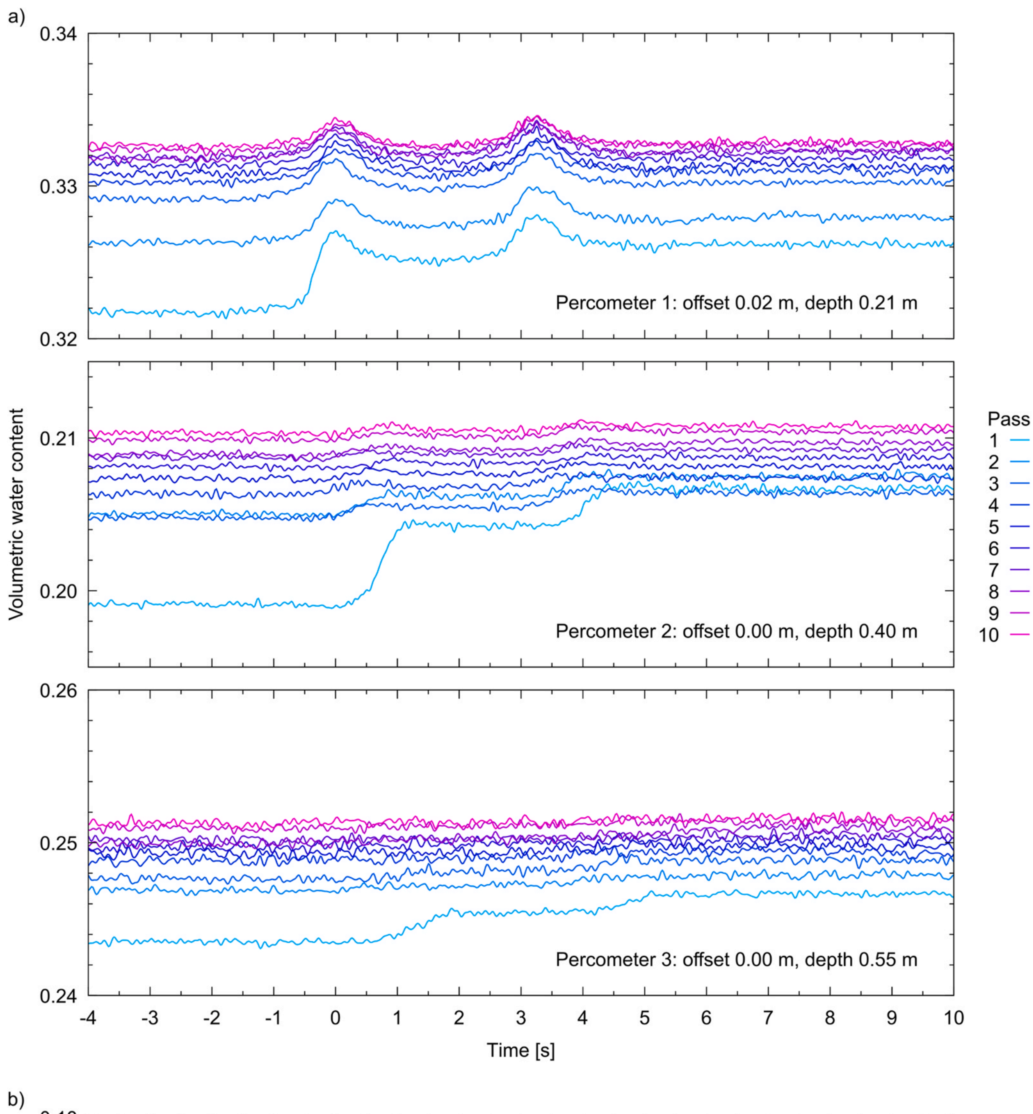

Fig. 5. Volumetric water content during the vehicle passes. Data sets were lowpass filtered, zero seconds was set to be the moment when the front axle of the vehicle is on the Percometer 1 (PM1) and vehicle speed was normalized in relation to the first pass of the vehicle. Subfigure a) presents the three Percometers (1–3) directly under wheels and subfigure b) is showing data from Percometer 4 (PM4) which was installed 0.35 m aside the wheel line. The offset from the travel line and the depth of each sensor are presented in subfigure labels.

vehicle passages. Tukey's test was used for multiple comparisons. A significance level of $p < 0.05$ was used in statistical testing. Normality of data was tested with Shapiro-Wilk's test, and homoscedasticity with Levene's test, both at a significance level of $p > 0.05$. Statistical analyses were performed with Python using the Stats module in the SciPy library (Virtanen et al., 2020).

3. Results and discussion

3.1. Continuous measurements during vehicle passes

Due to technical difficulties, the Bolling probe data from the first vehicle pass was lost. Bolling probe data sets from vehicle passes two to ten were lowpass filtered, $t = 0$ was set to be the moment when the front axle of the vehicle is on the Bolling probe 1 (BP1) and vehicle speeds were normalized in relation to the first pass of the vehicle. Fig. 4a presents the three Bolling probes (1−3) at the start of the sensor area with three different installation depths. Fig. 4b shows data from Bolling probe 4 (PM4) which was installed at the end of the sensor area to get data for the calculation of the vehicle speed. Note that the pressure decreased clearly with depth and the magnitude of pressures in probes 1 and 4 were comparable due to the similar sensor depths (Fig. 4).

Driving speed at compaction runs was in the range 0.71–0.82 m/s, as presented in Appendix Fig. C1. In this speed range, the measuring setup captures stress dynamics caused by the vehicular loading with high precision. Distinctive peaks from both axles of the tractor can be seen in data from all the installation depths as presented in lowpass filtered data sets in Fig. 4 and raw data examples in Appendix Fig. A1.

Bolling probe measurements from pass two were clearly distinguishable from passes three to ten. The shift of the base level in the pass two data was approximately ten times larger than that recorded at passes three to ten. This indicates that the increase in soil compaction and vehicular loading induced deformations were larger on the first two passes. The soil was still less dense and worked to a greater extent during the first two passes, enabling the pre-pressurized pressure-sensing silicone tube in the soil to create a larger space in soil. The pre-pressure must therefore be adequate to compensate for this. Similar shifts of base levels of Bolling probes as a function of vehicular passes have been previously reported by Schäffer et al. (2007). Soil compaction was also observed with soil porosity analyses from X-ray tomography images and water retention measurements performed in the laboratory (see below Fig. 8 and Fig. 11).

Percometer data sets from vehicle passes one to ten were lowpass filtered, shifted and normalized according to driving speed with the method presented in Section 2.4.1. The data described above were used to calculate volumetric water content with Eq. (3). Volumetric water content during the compaction runs is presented in Fig. 5. All Percometers showed a clear increase in soil moisture levels due to vehicular passes and loading.

Percometer 1 which was installed closest to the soil surface, at 0.21 m depth, presented an elastic soil behavior at measured soil moisture values (Fig. 5). There are higher peaks when the axles of the tractor are passing over the sensor, but the values get lower after the vehicular load shifts further from the sensor. Percometers 2–4, which were installed deeper or further away from the driving line, do not present similar peaks, but the volumetric water content level is shifting to a higher level when the tractor axles pass over them. This behavior is most distinguishable on Percometers 2 and 3 during the first pass. However, Percometer 2 shows minor peaks in later passes when the soil was already compacted.

Percometer 4, which was not directly under the tractor wheel path, also presented a small increase in soil moisture level as a function of vehicle passes. This was due to the tire loading induced pressure bulb causing soil compaction (Koolen and Kuipers, 1983), extending not merely to varying depth in soil but also outside tire width (Söhne, 1958). Percometer 4 results indicate that changes in volumetric water content measured by Percometers were more of the result of soil compaction and decreasing soil porosity than actual displacement or release of water in soil. This conclusion is also backed by a decrease in soil porosity observed in analyses made from water retention measurements and X-ray images (see below Fig. 8 and Fig. 11).

The driving speed of the tractor during the higher speed 11th pass was 4.26 m/s. Speed was calculated from Bolling probe data by the method presented in Section 2.4.1. Unfiltered Bolling probe pressure data from the high-speed tractor pass is presented in Fig. 6. Time values of data were shifted so that the front axle of the tractor was on the Bolling probe 1 (BP1) at zero seconds. Lowpass filtering was not used to ensure that high frequency details of the data were preserved and visible. Pressure scales of subfigures in Fig. 6 were set to the same as in Fig. 4 for the ease of comparison.

The most noticeable features of Bolling probe data from the higher speed tractor pass were oscillations of pressure on the sensors 1 and 4, closest to the soil surface. After an axle of the tractor had passed a sensor close to the surface and pressure had decreased from the peak value, pressure observed by the Bolling probe oscillated around the base level value with a frequency less than 20 Hz. The frequency was significantly lower than the frequency of our data sampling, which indicates that this was not related to our measuring method but is a real mechanical phenomenon in soil, caused by the tractor-soil system vibration triggered by wheel lugs.

Topsoil is deformed by the field traffic (Schjønning, 2023). Our observation indicates that field traffic can lead to additional soil compaction due to excited ground vibrations. Typically, the soil compaction in agricultural soil is considered to result from quasi-static loading, where the rut formation results from the weight of the vehicle traversing the soil (e.g. Ding et al., 2022). However, when the vehicle speed increases, also dynamic soil-tyre interactions resulting in soil vibrations can provide another compaction component (Hildebrand et al., 2008). Curiously, the observed frequence of pressure oscillations was close to a reported optimal compaction frequence for vibratory roller (Wersäll et al., 2016). In addition, the magnitude of peak values measured by the sensors BP1 and BP4 are approximately one third of the corresponding values measured by the same sensors with the lower tractor speed. Similar effects, i.e. oscillations or peak values lower than those of slower test drives, were not observed by Bolling probe sensors 2 and 3 located deeper in the soil. In addition, Percometers with a lower sampling frequency were unable to detect oscillations as the scarce samples were not able to catch the true waveform of the signal despite of being accurate as such. The above is presented in Appendix D, where the raw Percometer data from the high-speed pass are visualized. This also emphasizes the fact that said dynamic effects could not have been observed with previously reported stress measuring setups (Schäffer et al., 2007, Berisso et al., 2013), as they had even lower sampling frequencies.

3.2. Soil characterization

Soil bulk density increased significantly ($p < 10^{-6}$) due to compaction of soil (Fig. 7). Repeated vehicle passes resulted in further increase in bulk density (median bulk densities were 1.30, 1.37, and 1.47 cm^{-3} after 0, 2 and 10 passes, respectively). These results were as expected and similar behavior after repeated vehicle passes has been reported in previous studies (e.g. Patel and Mani, 2011). The bulk density values stayed below 1.5 in all measured samples, which indicates that the soil did not reach its maximum density. For example, the literature review reported considerably higher values for the bulk density of course-textured compacted topsoils (Zhang et al., 2024). Soil bulk density affects root growth and crop productivity. Root growth has been observed to have a bell-shaped response to bulk density, with the lowest and highest bulk densities being suboptimal for root growth (Alameda et al., 2012). In low bulk density soils, root growth can be reduced by insufficient root-to-soil contact, whereas high bulk density increases the

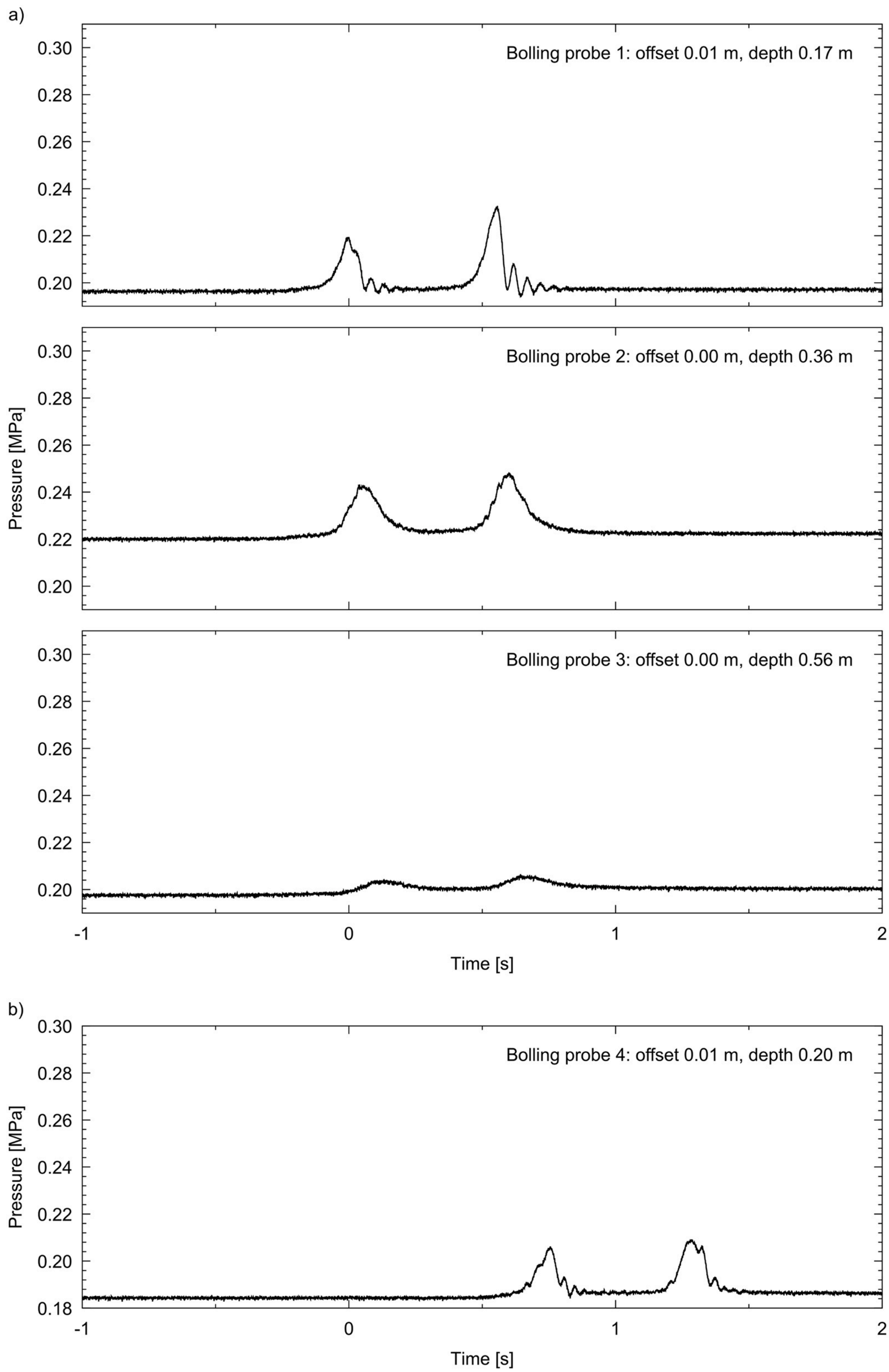

Fig. 6. Unfiltered data of Bolling probe measurements from the 11th pass with the higher vehicle speed. Time values of data are shifted in so that the front axle of the tractor is on the Bolling probe 1 (BP1) at zero seconds. The offset from the travel line and the depth of each sensor are presented in subfigure labels.

mechanical resistance to root growth and may lead to oxygen deficiency due to reduced air-filled macroporosity (Arvidsson, 1999, Tracy et al., 2012).

The total porosities determined from water retention measurements and porosities for pore size classes (pore diameter greater or smaller than 30 μm) are shown in Fig. 8. Measurements were done for soil sampled before the experiment and after 2 and 10 vehicle passes. A statistically significant reduction of total porosity from 49 % to 41 % ($p < 10^{-7}$) was observed with the number of vehicle passes increasing from 0 to 10. Concerning the large pores with the pore diameter

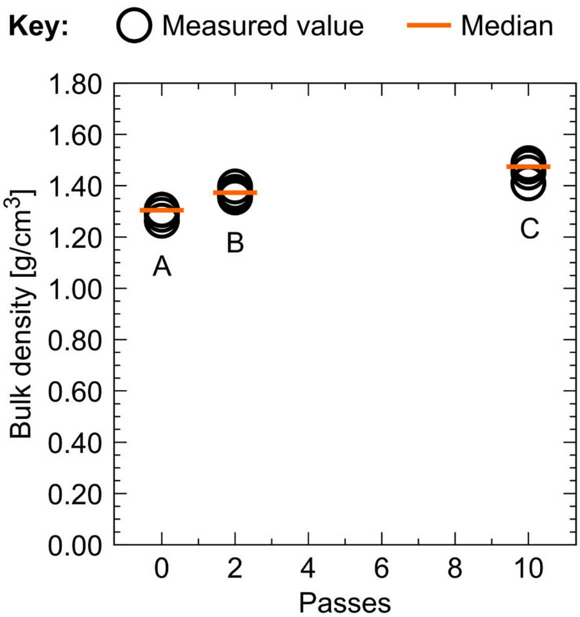

Fig. 7. Bulk densities of soil samples taken before vehicle passes and after two and ten passes. Statistically significant differences ($p < 0.05$; ANOVA and Tukey's test) from pairwise comparisons are denoted by different capital letters.

exceeding 30 µm, a similar decrease in porosity was detected (from 22 % to 8 %; $p < 10^{-6}$). On the contrary, the porosity of pores with a diameter smaller than 30 µm increased with increasing number of passes (from 26 % to 33 %; $p < 0.01$). The full pore size distributions utilizing all suctions used in the measurements are presented in Appendix E. These distributions show similar trends for all pore size classes below and above the ca. 30 µm point. These results indicate that the large pores collapsed due to the vehicular loading resulting in smaller sized pores.

Volumetric soil moisture content was also directly determined from water retention samples. The results are shown in Fig. 9. These results show that the moisture content increased from 0.25 to 0.30 ($p < 10^{-7}$). These values are comparable to those that were measured with Percometers (Fig. 5) and show a similar increase in moisture with an increasing number of vehicle passes. One explanation for the moisture increase could be the reduction of air-filled macroporosity and an increase in the volume of smaller pores responsible for water storage in soil (Pagliai and Vignozzi, 2002). However, since soil sampling was conducted immediately after the vehicle passes, the soil was likely in a state of nonequilibrium where the soil moisture and water suction do not follow a unique water retention curve (e.g. Vogel et al., 2023). Thus, the moisture increase may result from the reduction of the pore volume due to compaction. Generally, soil compaction is affected by the soil moisture content (Nawaz et al., 2013). A soil with a lower moisture content is less prone to compaction than the same soil at a higher moisture level. The soil vulnerability to compaction increases with the soil moisture up to a moisture limit (Nawaz et al., 2013; Fu et al., 2019).

The soil pore structure was also analyzed with X-ray tomography. Visual examples of X-ray-imaged soil samples are shown in Fig. 10. The shown cross-sections demonstrate the compaction process that occurred in the soil. The mineral particles in the soil were more densely packed after the vehicle passes, whereby the total porosity was reduced and the largest pores diminished. The properties of whole segmented 3D image stacks were quantified with image analysis. The porosities visible in X-ray images are shown in Fig. 11a. Image analysis results showed a comparable decreasing trend (from 20 % to 9 %; $p < 0.01$) as water retention measurements for pore diameters exceeding 30 µm. Note that the 30 µm pore diameter approximately corresponds to the imaging resolution. Considering the pore size, the median pore diameter determined from the pore size distributions determined from images showed a decreasing trend from 96 µm to 73 µm ($p < 0.01$; see Fig. 11b). While the porosity results from X-ray tomography images match quite well with the porosity of pores with a diameter exceeding 30 µm, there are different underlying assumptions in the methods which prevent a fully reliable comparison. For example, conversion of the water retention measurement results to porosity is based on the Young-Laplace equation and capillary bundle model (Bachmann and van der Ploeg, 2002) with assumptions which are not fully valid for the soil pore systems. On the other hand, while the voxel size in imaging was 30 µm, the size of the pores that can be resolved from the images is somewhat larger.

Previous studies considering soil porosity after vehicle loading have shown similar results. For example, Sandin et al. (2017) showed a comparable decrease in porosity visible in X-ray images when comparing wheel tracks and non-trafficked soil at a clay loam field. Keller et al. (2019) also reported a similar reduction in the imaged macroporosity after compaction in a loamy soil. While the soil textures in both the above-mentioned studies were finer than in our soil and the vehicles used were different, the immediate impacts of loading on the soil macroporosity were similar to ours. Previous studies on sandy soils have also reported similar trends of macroporosity reduction. For

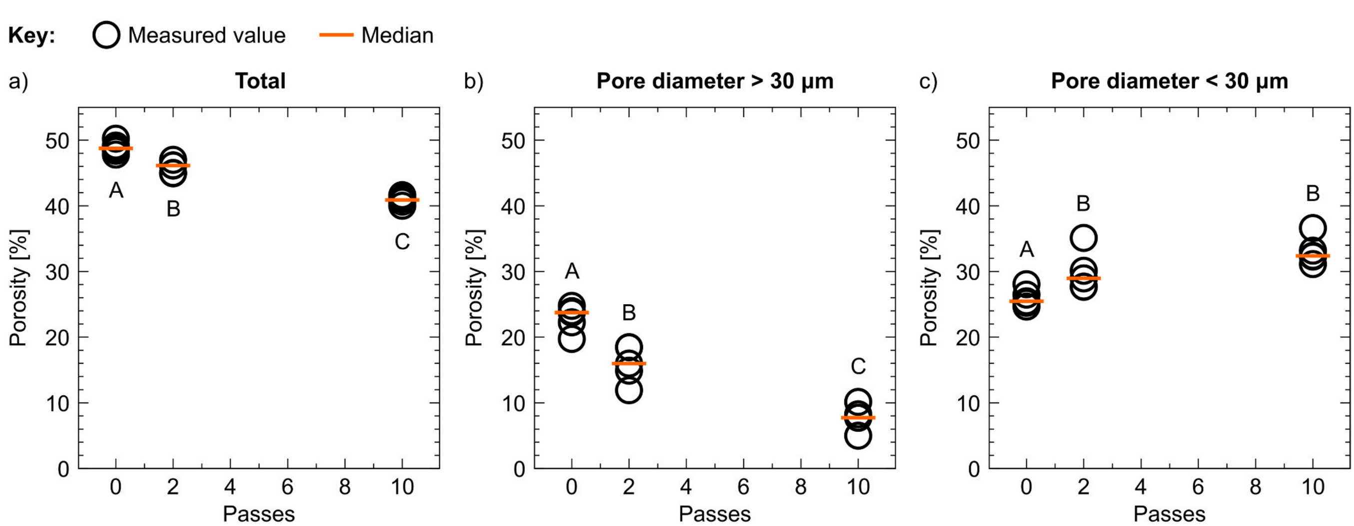

Fig. 8. Soil porosities before loading and after 2 and 10 vehicle passes. Porosities are derived from water retention measurements: (a) Total porosity, (b) pore diameter > 30 µm, (c) pore diameter < 30 µm. Statistically significant differences ($p < 0.05$; ANOVA and Tukey's test) from pairwise comparisons within each panel are denoted by different capital letters.

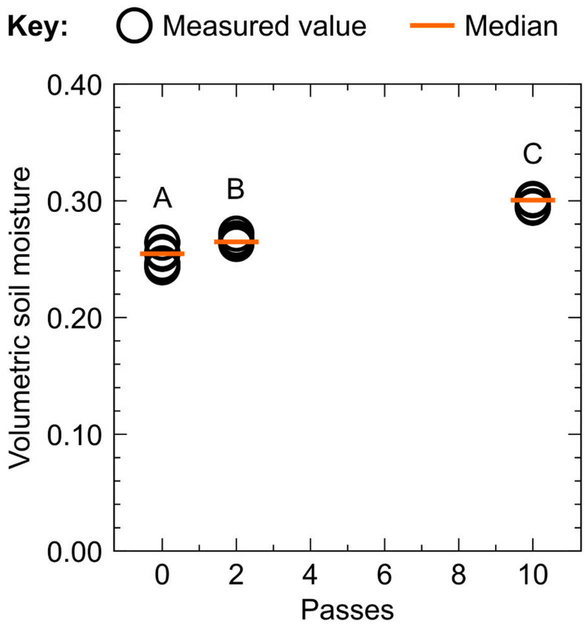

Fig. 9. Volumetric soil moisture before loading and after 2 and 10 vehicle passes. Statistically significant differences ($p < 0.05$; ANOVA and Tukey's test) from pairwise comparisons are denoted by different capital letters.

example, Fu et al. (2019) studied compaction of a loamy sand at different moisture contents using a light steel roller to compact the soil. They reported a porosity reduction with the number of passes, which depended on the soil moisture status. They also found a shift in the pore size distribution such that the volume of large pores was reduced while the share of smaller ones increased (Fu et al., 2019). Calleja-Huerta et al. (2023), in turn, studied the compaction of a loamy sand caused by a light-weight field robot. They observed a reduction in the effective air-filled porosity and air permeability due to field traffic and suggested that this change resulted from the rearrangement of soil particles and consequent reduction in soil porosity. Compaction of sand loam caused by a tractor-trailer combination was studied by ten Damme et al. (2021), whose results showed a trend towards a larger share of smaller pores (<30 μm) and partial disruption of macropores. The results from our experiments are in line with these previous experiments conducted on coarse mineral soils. Even though a wide range of vehicles has been used in these studies, the qualitative behaviour consistently shows a macropore reduction, which suggest that macroporosity is more sensitive to soil deformation and that these changes may lead to an increase in the volume of smaller pore sizes despite the reduction of total porosity. Here we considered the structural characteristics of the topsoil layer only. It is well known that the compaction effect of vehicle load can reach deeper soil layers (Alakukku and Elonen, 1994; Etana and Håkansson, 1994) and a similar cumulative effect of repeated vehicle passes has been detected (Patel and Mani, 2011).

Only minor rut formation not exceeding the tire lug height resulted from tractor passes. The average measured rut depth after 2 and 10 passes was 1.6 cm and 2.5 cm, respectively. Soil penetration resistance results are shown in Fig. 12. Soil penetration resistance increased with the number of tractor passes in ploughed topsoil at 0–18 cm depth. In this layer, the statistical significance of the differences was tested with ANOVA at depths of 5 and 15 cm. At 5 cm depth, the difference between the cases with 0, 2 and 10 passes were all significant whereas at 15 cm depth, the penetration resistance after 2 and 10 passes differed significantly. At 25 cm depth, no statistically significant differences were detected whereas from 30 cm to 50 cm depth, the penetration resistance after 10 passes was significantly lower than in the cases of 0 and 2 passes according to ANOVA. The variation of penetration resistance over spatial length scales from centimeters to meters has been reported (Kılıç et al., 2004; Usowicz and Lipiec, 2009). However, due to our considerable number of measurements and statistical testing of the resulting data set, the probability for the seen effect to be only variation in penetrometer resistance should be small. Nevertheless, the behavior of the 30–50 cm layer could not be explained on the basis of the results.

The results of the shear strength tests are shown in Fig. 13. The function described in Section 2.4.4 was fitted to the data sets. The resulting linear relationships are presented in Fig. 13 and fitted parameters in Table 1. Based on the shear strength test results, the studied soil possessed both cohesive and frictional properties as could be expected from a loamy sand soil. The values of cohesion and angle of internal friction are in reasonable agreement with the values reported for sandy clay loam by Stafford and Tanner (1982), for sandy loam by Ala-Ilomäki (1993) and for clayey sand by Afolabi and Afolayan (2018). Measured shear strength increased with increasing number of passes at the studied range of normal stress. The cohesion of the soil samples increased as a function of the number of passes indicating increasing bulk density and state of compaction. This is in agreement with measured compaction due to vehicular loading. A slight yet not significant decrease in the angle of internal friction was observed with increasing number of passes.

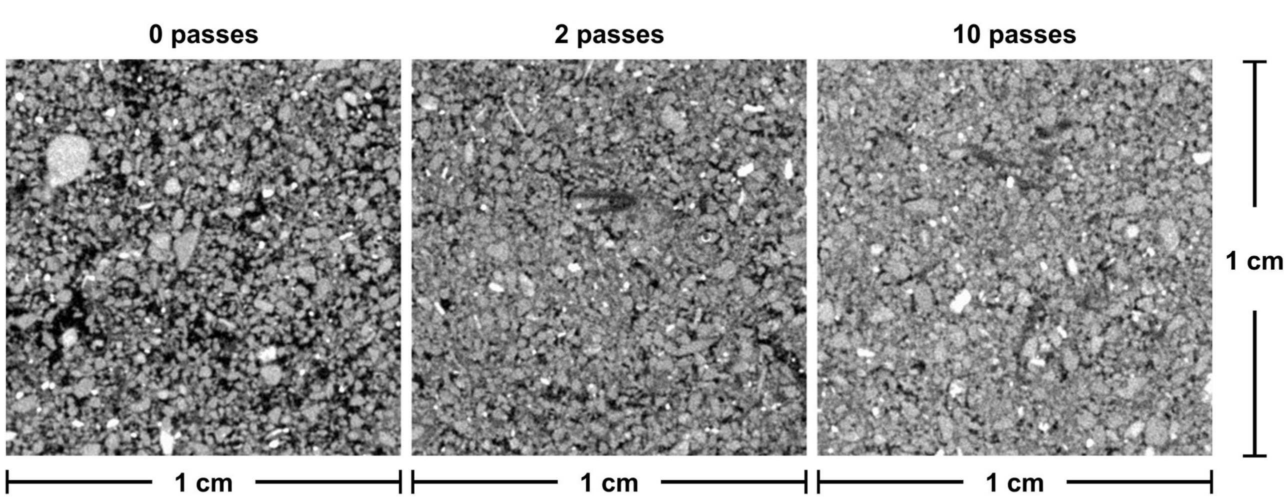

Fig. 10. Three example cross-sections from X-ray-imaged soil samples. The shown cross-sections are from the soil before the experiment and after 2 and 10 vehicle passes. A darker color indicates lower material density and higher density results appear as lighter color, whereby pores are shown in black. The size of each cross-section is 1 cm x 1 cm corresponding to a small subdomain of the whole sample cross-section.

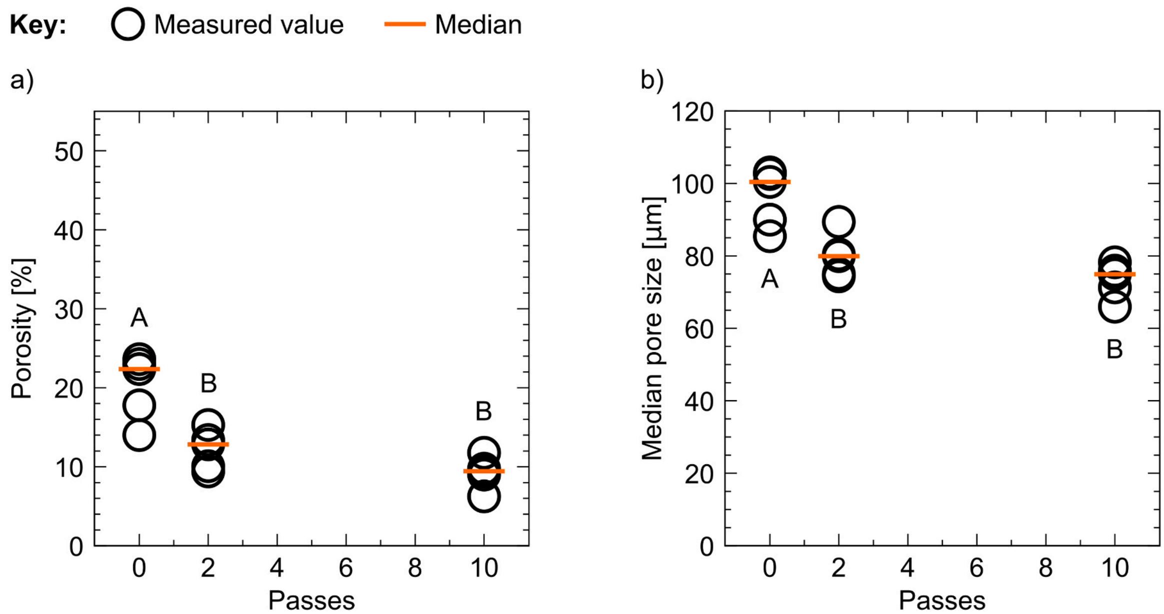

Fig. 11. (a) Soil porosity and (b) median pore diameter determined from X-ray tomography images for samples taken before the experiment and after 2 and 10 vehicle passes. Statistically significant differences ($p < 0.05$; ANOVA and Tukey's test) from pairwise comparisons are denoted by different capital letters.

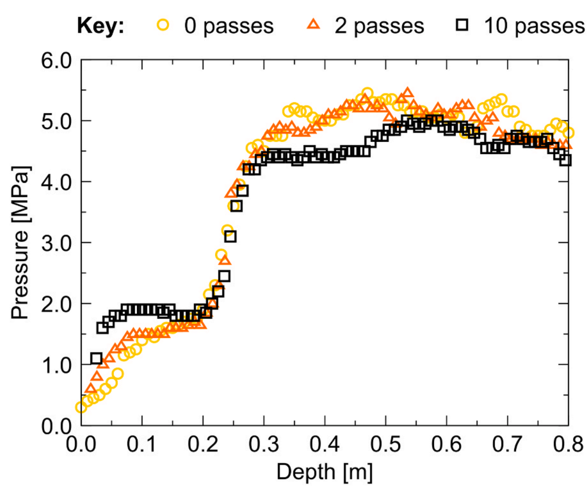

Fig. 12. Median of penetrometer measurements before the vehicle passes, after two passes and ten passes. Depth values of data sets concerning two and ten passes were shifted according to average rut depths measured from the test trail.

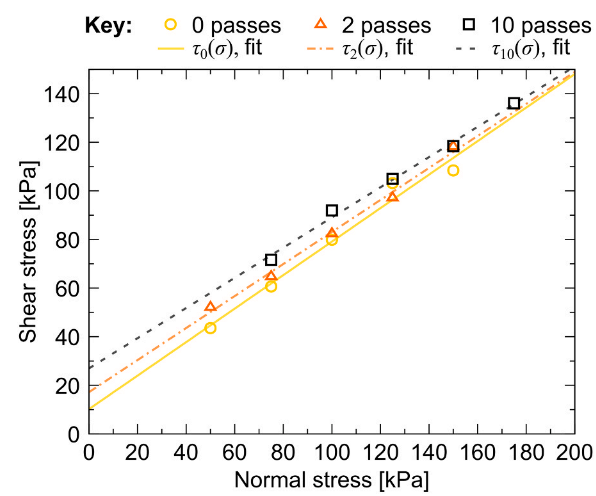

Fig. 13. Shear stress values were measured from samples taken before the vehicle passes and after two and ten passes. The linear function described in Eq. (4) was fitted to experimental data. Fitted parameter values are presented in Table 1.

4. Conclusions

Results from the Bolling probe measurements clearly present the capabilities of our high-sampling-rate measurement setup in investigating the effects of vehicle-terrain interaction on soil. With the sampling rate in kHz region, Bolling probes provide detailed data on the stress state in soil during a loading process induced by a vehicular pass. In addition, data collected from the tractor pass with the higher speed showed the exact reason why the high sampling rate is needed. Highly dynamic effects, such as oscillations observed with our Bolling probe setup, would have been undetectable with a lower frequency, as presented by Percometer data from the same vehicle pass. An additional advantage of the Bolling probes is their relative ease of installation into the soil. Also, the performed Percometer measurements proved to be a valuable method for the investigation of soil moisture state and dynamics when vehicle passes at slower speeds were studied.

The dynamic measurements were supported by laboratory analyses showing consistent results. The volumetric soil moisture content determined using undisturbed soil samples from the test track supported the Percometer measurements showing an increase in moisture with an increasing number of vehicle passes. Bulk density analyses and X-ray

Table 1
Fitted parameter values for the linear function described in Eq. (4). The function was fitted to experimental data from shear stress measurements performed for samples taken before the vehicle passes and after two and ten passes. Error values presented for fitted parameters are asymptotic standard errors. The internal angle of friction for each data set was calculated from the fitted slope.

Passes	C [kPa]	$\tan(\phi)$	ϕ[deg]
0	10.19 ± 6.78	0.69 ± 0.07	35 ± 4
2	17.20 ± 3.33	0.66 ± 0.04	33 ± 2
10	26.94 ± 3.67	0.62 ± 0.03	32 ± 2

tomography imaging showed that the structural changes during the first two tractor passes were greater than after that up to 10 passes. The pore size analyses showed that loading led to a reduction of the macroporosity (>30 μm) and a simultaneous increase in smaller-scale porosity.

An increase in soil volumetric water content with increasing number of passes was observed with the Percometer measurements and in the laboratory soil analysis. As the bulk density according to the laboratory analysis also increased and the porosity according to the X-ray tomography decreased with increasing number of passes, it can be assumed that the Percometer results are due to soil compaction.

The penetration resistance in the soil layer 0–20 cm increased with increasing number of tractor passes, as could be expected. By contrast, the decrease in penetration resistance at soil depth of 30–50 cm with 10 tractor passes was unexpected. Considering the substantial number of measurements, 36 measurements before passes, after 2nd and after 10th pass, erroneous measurement results are unlikely, yet this should be studied more in detail in the future.

Our experiment with high-sampling-rate Bolling probe sensors and continuous Percometer measurements showed the effectiveness of both methods and agreement of results with laboratory analyses. They also demonstrated the necessity of the high sampling rate when investigating dynamic effects in soil caused by a vehicular pass with normal operating speed.

To conclude, the presented experimental approach provides new opportunities to investigate soil compaction, which is a severe threat to soil physical health. The measurements with a high sampling rate also enable studies of soil rheology under field conditions. To fully comprehend the loading process and its consequences, extensive field studies covering a wide spectrum of soil types, moisture conditions, soil management practices, different running gear configurations and operating speeds should be organized.

CRediT authorship contribution statement

Jari Ala-Ilomäki: Writing – original draft, Resources, Methodology, Investigation, Conceptualization. **Jari Hyväluoma:** Writing – original draft, Visualization, Methodology, Investigation, Formal analysis, Conceptualization. **Harri Lindeman:** Writing – original draft, Project administration, Methodology, Investigation, Conceptualization. **Mika Tähtikarhu:** Writing – review & editing, Investigation. **Johanna Nikama:** Writing – review & editing, Investigation. **Jukka Kuva:** Writing – review & editing, Investigation. **Sampo Kulju:** Writing – original draft, Visualization, Methodology, Investigation, Formal analysis, Conceptualization.

Declaration of Competing Interest

The authors declare that they have no known competing financial interests or personal relationships that could have appeared to influence the work reported in this paper.

Acknowledgements

This work was supported by Luke strategic funding for the MobiTraf project. X-ray tomography was funded by the Research Council of Finland via the RAMI infrastructure project [grant number 293019]. CSC–IT Center for Science is acknowledged for computing time. We are grateful to Niko Jalava for technical assistance.

Appendix A. Bolling probe and Percometer raw data examples

Raw data of Bolling probe measurements from vehicle pass two is presented in Fig. A1.

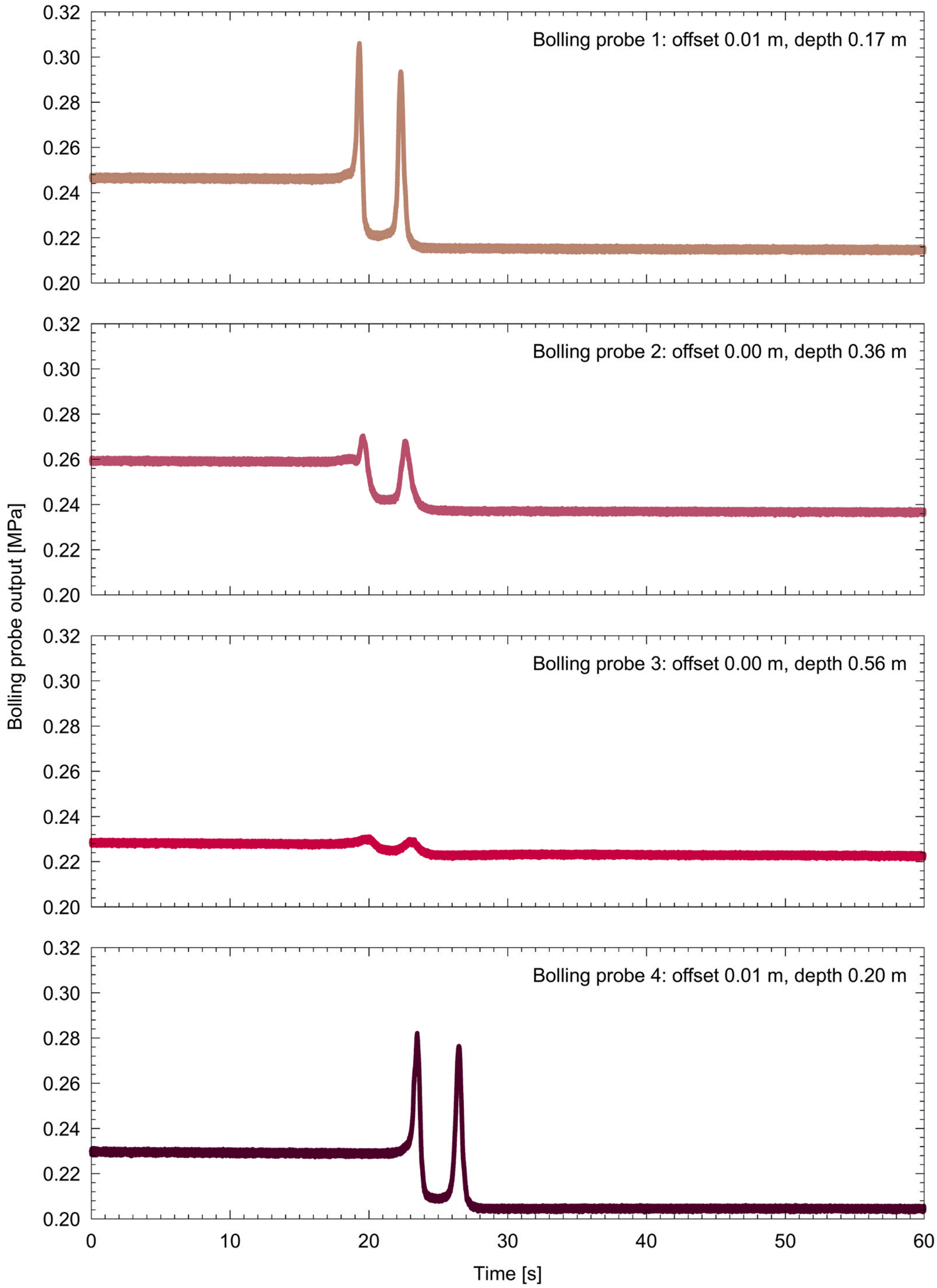

Figure A1. Raw data of Bolling probe measurements from vehicle pass two

Raw data of Percometer measurements from vehicle pass one is presented in Fig. A2.

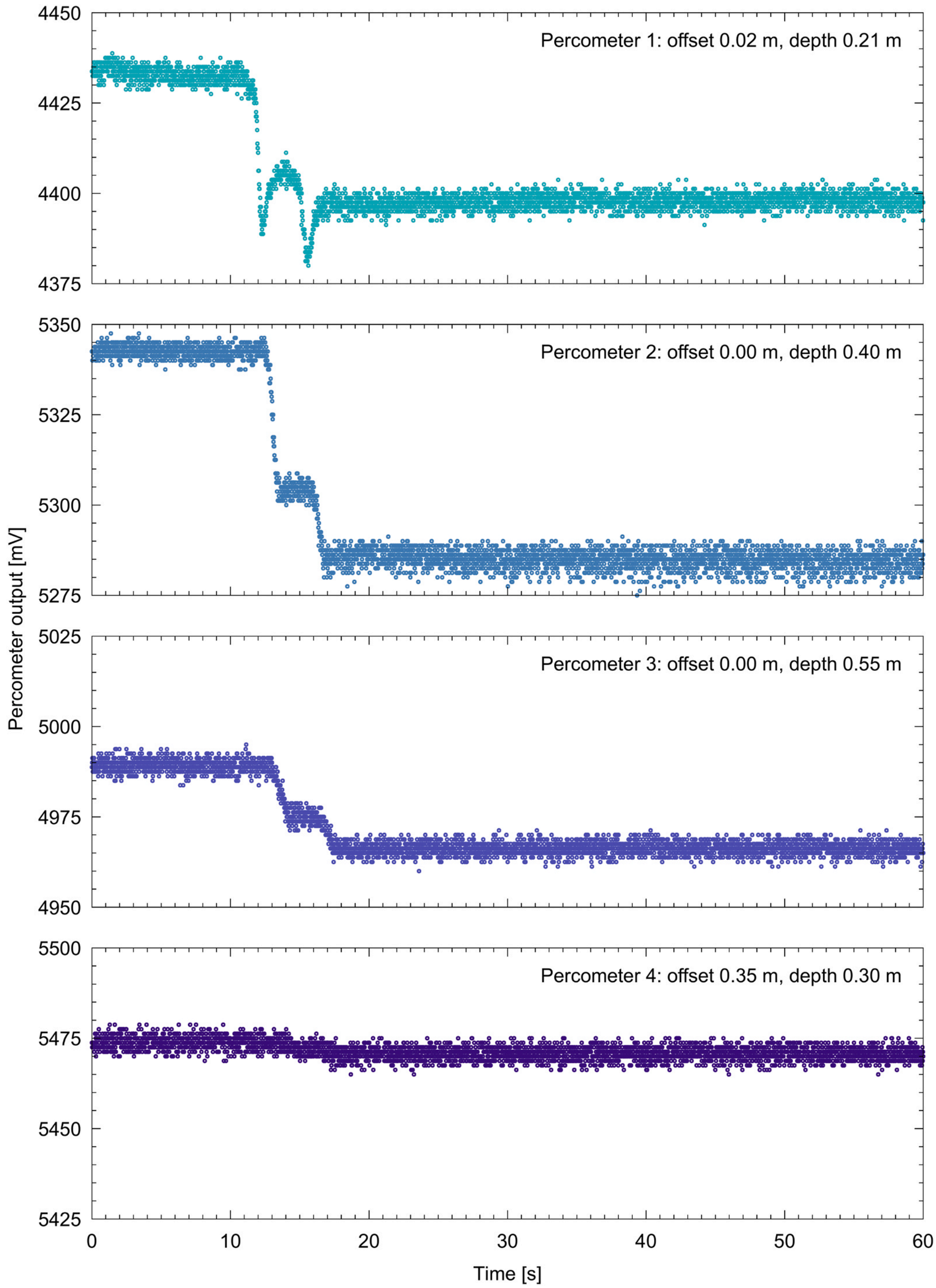

Figure A2. Raw data of Percometer measurements from vehicle pass one

Appendix B. Percometer calibration data

The calibration data, from output values in mV to dielectric constant ε_R, of Percometer 1 (PM1) is presented in Fig. B1.

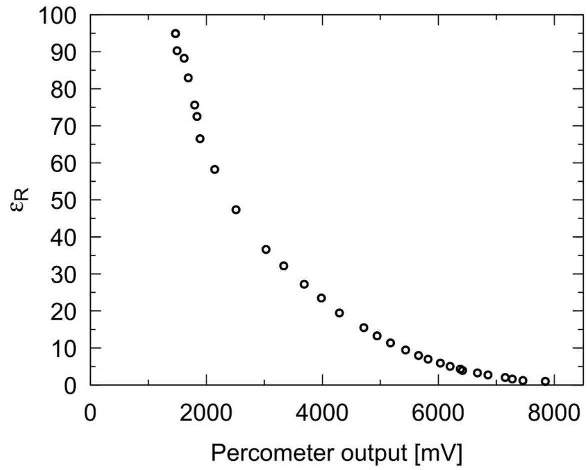

Figure B1. Calibration data of Percometer 1 (PM1) presenting a conversion from output values in mV to dielectric constant ε_R

Appendix C. Speed of the tractor for ten compaction passes

The speed of the vehicle for each ten compaction passes was calculated from low pass filtered Percometer data. Speed values are presented in Fig. C1.

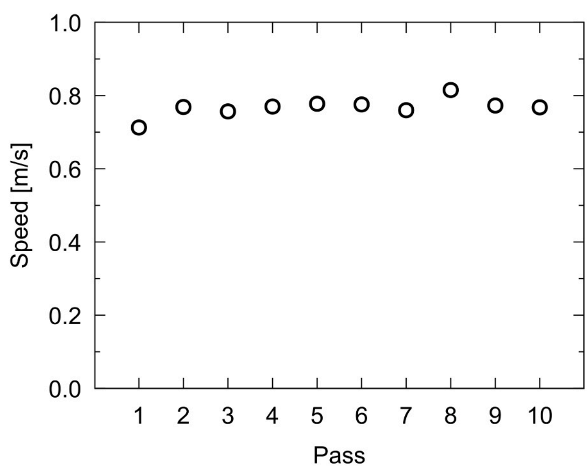

Figure C1. Speed of the vehicle for each compaction pass

Appendix D. Percometer raw data from the 11th pass with a high vehicle speed

Raw data of Percometer measurements from the 11th vehicle pass with a high vehicle speed is presented in Fig. D1. Data is visualized with line plots for easier reading.

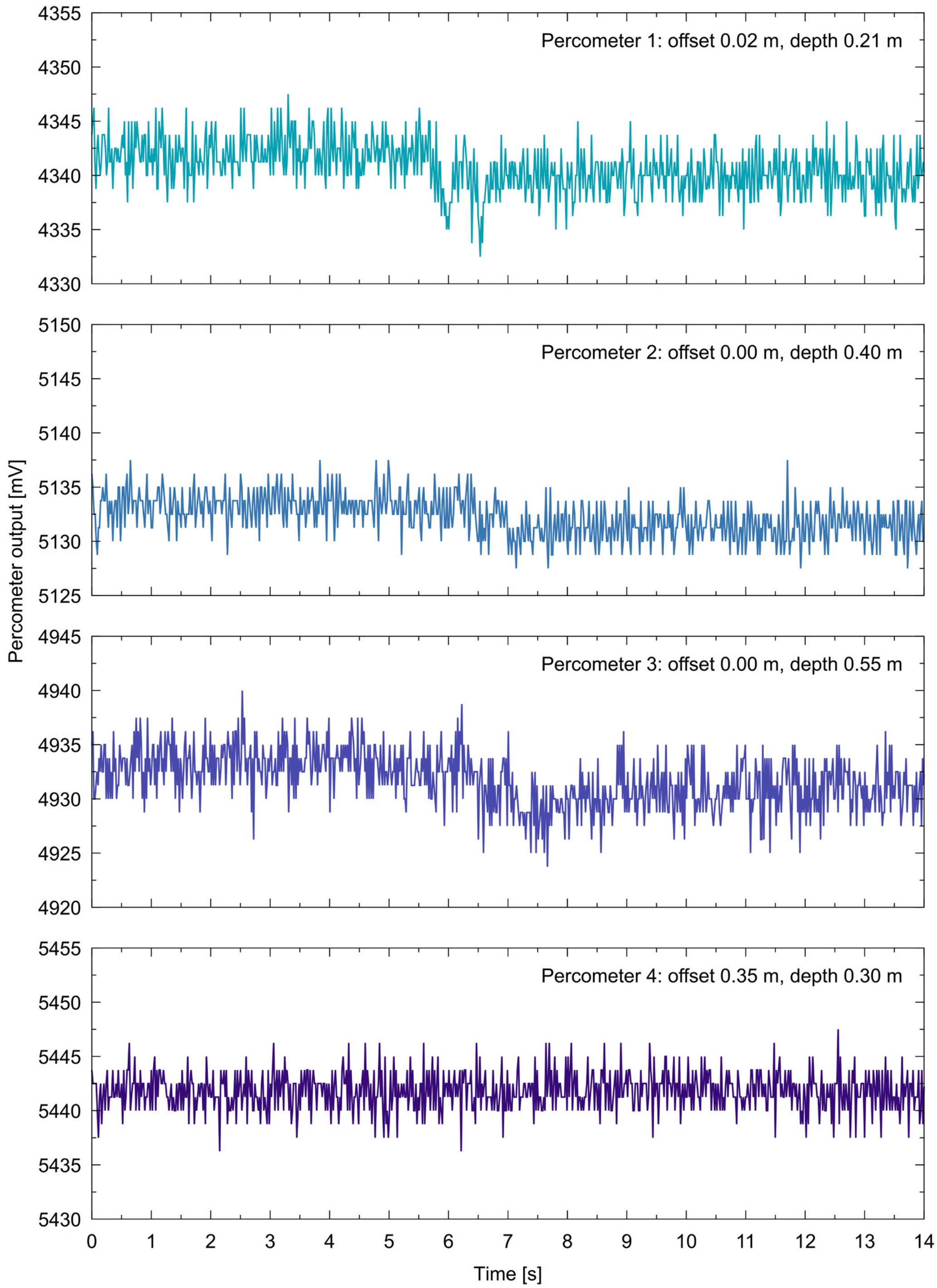

Figure D1. Percometer raw data from the 11th pass with a high vehicle speed

Appendix E. Soil pore size distributions from the water retention measurements

Porosities of all pore size classes available from the water retention curves is shown in Table E1.

Table E1
Pore size distributions derived from water retention measurements. Statistically significant differences ($p < 0.05$) from pairwise comparisons within rows are denoted by different capital letters for those size ranges for which ANOVA showed statistically significant results ($p < 0.05$)

Mean porosity

(*continued on next page*)

Table E1 (*continued*)

	Mean porosity		
Pore size range [μm]	0 passes	2 passes	10 passes
Total porosity	48.9 A	45.8 B	40.9 C
< 0.2	4.9 A	5.2 B	5.5 C
0.2–1	11.8	13.4	16.5
1–3	2.0 A	3.2 A	3.3 B
3–30	7.3	8.1	7.8
30–100	10.7 A	10.7 A	6.0 B
100–300	10.2 A	4.3 B	1.3 C
300–1200	2.1 A	0.6 AB	0.0 B
> 1200	0.0 A	0.4 B	0.4 B

Data availability

The X-ray tomography data are available at https://doi.org/10.23729/b326fe8a-2627–491e-ae2f-2df308c1cc73 under CC BY 4.0 license.

References

Afolabi, O.A., Afolayan, O.D., 2018. Strength modelling of soil geotechnical properties from index properties. Jordan J. Civ. Eng. 12 (4), 619–628.
Ala-Ilomäki, J., 1993. A terramechanical approach for evaluating mobility and ground disturbance during skidding and forwarding: preliminary trials. For. Eng. Inst. Can. Special Report SR-86. 14.
Alakukku, L., Elonen, P., 1994. Finnish experiments on subsoil compaction by vehicles with high axle load. Soil Tillage Res. 29, 151–155. https://doi.org/10.1016/0167-1987(94)90051-5.
Alakukku, L., Weisskopf, P., Chamen, W.C.T., Tijink, F.G.J., van der Linden, J.P., Pires, S., Sommer, C., Spoor, G., 2003. Prevention strategies for field traffic-induced subsoil compaction: a review Part 1. Machine/soil interactions. Soil Tillage Res. 73 (1–2), 145–160. https://doi.org/10.1016/S0167-1987(03)00107-7.
Alameda, D., Anten, N.P.R., Villar, R., 2012. Soil compaction effects on growth and root traits of tobacco depend on light, water regime and mechanical stress. Soil Tillage Res. 120, 121–129. https://doi.org/10.1016/j.still.2011.11.013.
Arvidsson, J., 1999. Nutrient uptake and growth of barley as affected by soil compaction. Plant Soil 208, 9–19.
Arvidsson, J., Håkansson, I., 1996. Do effects of soil compaction persist after ploughing? Results from 21 long-term field experiments in Sweden. Soil Tillage Res. 39, 175–197.
Bachmann, J., van der Ploeg, R.R., 2002. A review on recent developments in soil water retention theory: interfacial tension and temperature effects. J. Plant Nutr. Soil Sci. 165, 468–478.
Berisso, F.E., Schjønning, P., Lamandé, M., Weisskopf, P., Stettler, M., Keller, T., 2013. Effects of the stress field induced by a running tyre on the soil pore system. Soil Tillage Res. 131, 36–46. https://doi.org/10.1016/j.still.2013.03.005.
Brus, D.J., van den Akker, J.J.H., 2018. How serious a problem is subsoil compaction in the Netherlands? A survey based on probability sampling. SOIL 4 (1), 37–45. https://doi.org/10.5194/soil-4-37-2018.
Calleja-Huerta, A., Lamandé, M., Green, O., Munkholm, L.J., 2023. Impacts of load and repeated wheeling from a lightweight autonomous field robot on the physical properties of a loamy sand soil. Soil Tillage Res. 233, 105791. https://doi.org/10.1016/j.still.2023.105791.
Cambi, M., Certini, G., Neri, F., Marchi, E., 2015. The impact of heavy traffic on forest soils: a review. For. Ecol. Manag. 338, 124–138. https://doi.org/10.1016/j.foreco.2014.11.022.
Chen, X., Cruse, R.M., Niu, S., Zhang, S., 2019. Effect of loading time on soil structural failure. Soil Tillage Res. 186, 87–93. https://doi.org/10.1016/j.still.2018.10.001.
ten Damme, L., Schjønning, P., J. Munkholm, L., Green, O., K. Nielsen, S., Lamandé, M., 2021. Soil structure response to field traffic: effects of traction and repeated wheeling. Soil Tillage Res. 213, 105128. https://doi.org/10.1016/j.still.2021.105128.
DeArmond, D., Emmert, F., Lima, A.J.N., Higuchi, N., 2019. Impacts of soil compaction persist 30 years after logging operations in the Amazon Basin. Soil Tillage Res. 189, 207–216. https://doi.org/10.1016/j.still.2019.01.010.
Ding, Z., Munkholm, L.J., ten Damme, L., Lamandé, M., 2022. Vertical and horizontal soil stresses beneath a modern combine harvester: measurements and modelling. Land Degrad. Dev. 33 (6), 892–903. https://doi.org/10.1002/ldr.4191.
Elonen, P., 1971. Particle-size analysis of soil. Acta Agric. Fenn. 122, 1–122.
Etana, A., Håkansson, I., 1994. Swedish experiments on the persistence of subsoil compaction caused by vehicles with high axle load. Soil Tillage Res. 29, 167–172. https://doi.org/10.1016/0167-1987(94)90053-1.
Fu, Y., Tian, Z., Amoozegar, A., Heitman, J., 2019. Measuring dynamic changes of soil porosity during compaction. Soil Tillage Res. 193, 114–121. https://doi.org/10.1016/j.still.2019.05.016.
Geological Survey of Finland 2015. The Superficial deposits 1:20 000/1:50 000 data. https://tupa.gtk.fi/paikkatieto/meta/maapera_20_50k.html.
Ghadernejad, K., Shahgholi, G., Mardani, A., Chiyaneh, H.G., 2018. Prediction effect of farmyard manure, multiple passes and moisture content on clay soil compaction using adaptive neuro-fuzzy inference system. J. Terramechanics 77, 49–57. https://doi.org/10.1016/j.jterra.2018.03.002.
Gonzalez, R.C., Woods, R.E., 2008. Digital Image Processing, 3rd ed.). Pearson Education International.
Hamza, M.A., Anderson, W.K., 2005. Soil compaction in cropping systems: a review of the nature, causes and possible solutions. Soil Tillage Res. 82, 121–145.
Hildebrand, R., Keskinen, E., Navarrete, J.A.R., 2008. Vehicle vibrating on a soft compacting soil half-space: ground vibrations, terrain damage, and vehicle vibrations. J. Terra 45 (4), 121–136. https://doi.org/10.1016/j.jterra.2008.09.003.
Horgan, G.W., 1998. Mathematical morphology for analysing soil structure from images. Eur. J. Soil Sci. 49, 161–173. https://doi.org/10.1046/j.1365-2389.1998.00160.x.
Keller, T., Colombi, T., Ruiz, S., Schymanski, S.J., Weisskopf, P., Koestel, J., Sommer, M., Stadelmann, V., Breitenstein, D., Kirchgessner, N., Walter, A., Or, D., 2021. Soil structure recovery following compaction: short-term evolution of soil physical properties in a loamy soil. Soil Sci. Soc. Am. J. 85 (4), 1002–1020. https://doi.org/10.1002/saj2.20240.
Keller, T., Lamandé, M., 2010. Challenges in the development of analytical soil compaction models. Soil Tillage Res. 111 (1), 54–64. https://doi.org/10.1016/j.still.2010.08.004.
Keller, T., Ruiz, S., Stettler, M., Berli, M., 2016. Determining soil stress beneath a tire: measurements and simulations. Soil Sci. Soc. Am. J. 80 (3), 541–553. https://doi.org/10.2136/sssaj2015.07.0252.
Keller, T., Sandin, M., Colombi, T., Horn, R., Or, D., 2019. Historical increase in agricultural machinery weights enhanced soil stress levels and adversely affected soil functioning. Soil Tillage Res. 194. https://doi.org/10.1016/j.still.2019.104293.
Kılıç, K., Özgöz, E., Akbas, F., 2004. Assessment of spatial variability in penetration resistance as related to some soil physical properties of two fluvents in Turkey, 2004, Pages Soil Tillage Res. 76 (1), 1–11. https://doi.org/10.1016/j.still.2003.08.009.
Koolen, A.J., Kuipers, H., 1983. Agricultural soil mechanics. Advanced Series in Agricultural Sciences 13. Springer-Verlag, p. 241. ISBN: 3-540-12257-5.
Larsbo, M., Koestel, J., Jarvis, N., 2014. Relations between macropore network characteristics and the degree of preferential solute transport. Hydrol. Earth Syst. Sci. 18 (12), 5255–5269. https://doi.org/10.5194/hess-18-5255-2014.
Nawaz, M.F., Bourrié, G., Trolard, F., 2013. Soil compaction impact and modelling. A review. Agron. Sustain. Dev. 33 (2), 291–309. https://doi.org/10.1007/s13593-011-0071-8.
Pagliai, M., Vignozzi, N., 2002. The soil pore system as an indicator of soil quality. Adv. Geoecol. 35, 69.
Patel, S.K., Mani, I., 2011. Effect of multiple passes of tractor with varying normal load on subsoil compaction. J. Terra 48 (4), 277–284. https://doi.org/10.1016/j.jterra.2011.06.002.
Sandin, M., Koestel, J., Jarvis, N., Larsbo, M., 2017. Post-tillage evolution of structural pore space and saturated and near-saturated hydraulic conductivity in a clay loam soil. Soil Tillage Res. 165, 161–168. https://doi.org/10.1016/j.still.2016.08.004.
Schäffer, B., Attinger, W., Schulin, R., 2007. Compaction of restored soil by heavy agricultural machinery-Soil physical and mechanical aspects. Soil Tillage Res. 93 (1), 28–43. https://doi.org/10.1016/j.still.2006.03.007.
Schjønning, P., 2023. An empirical model for prediction of topsoil deformation in field traffic. Soil Tillage Res. 227, 105589. https://doi.org/10.1016/j.still.2022.105589.
Schjønning, P., van den Akker, J.J.H., Keller, T., Greve, M.H., Lamandé, M., Simojoki, A., Stettler, M., Arvidsson, J., Breuning-Madsen, H., 2015. Driver-Pressure-State-Impact-Response (DPSIR) analysis and risk assessment for soil compaction-A European perspective. Adv. Agron. 133, 183–237. https://doi.org/10.1016/bs.agron.2015.06.001.
Shahgholi, G., Abuali, M., 2015. Measuring soil compaction and soil behavior under the tractor tire using strain transducer. J. Terramechanics 59, 19–25. https://doi.org/10.1016/j.jterra.2015.02.007.
Söhne, W., 1958. Fundamentals of pressure distribution and soil compaction under tractor tires. Agric. Eng. 39, 290.
Stafford, J.V., Tanner, D.W., 1982. Field Meas. Soil Shear Strength a N. Des. Field Shear Meter.
Toivio, J., Helmisaari, H., Palviainen, M., Lindeman, H., Ala-Ilomäki, J., Sirén, M., Uusitalo, J., 2017. Impacts of timber forwarding on physical properties of forest soils in southern Finland. For. Ecol. Manag. 405, 22–30. https://doi.org/10.1016/j.foreco.2017.09.022.

Topp, G.C., Davis, J.L., Annan, A.P., 1980. Electromagnetic determination of soil water content: measurements in coaxial transmission lines. Water Resour. Res. 16 (3), 574–582.

Tracy, S.R., Black, C.R., Roberts, J.A., McNeill, A., Davidson, R., Tester, M., Samec, M., Korošak, D., Sturrock, C., Mooney, S.J., 2012. Quantifying the effect of soil compaction on three varieties of wheat (Triticum aestivum L.) using X-ray Micro Computed Tomography (CT). Plant Soil 353 (1–2), 195–208. https://doi.org/10.1007/s11104-011-1022-5.

Turpeinen, T., 2015. Analysis of microtomographic images of porous heterogeneous materials. Jyväskylä Stud. Comput. 230 https://jyx.jyu.fi/dspace/handle/123456789/48021.

Turunen, M., Hyväluoma, J., Heikkinen, J., Keskinen, R., Kaseva, J., Koestel, J., Rasa, K., 2019. Quantifying physical properties of three sphagnum -based growing media as affected by drying – wetting cycles. Vadose Zone J. 18, 190033. https://doi.org/10.2136/vzj2019.04.0033.

Usowicz, B., Lipiec, J., 2009. Spatial distribution of soil penetration resistance as affected by soil compaction: the fractal approach, 2009, Pages Ecol. Complex. 6 (3), 263–271. https://doi.org/10.1016/j.ecocom.2009.05.005.

Virtanen, P., Gommers, R., Oliphant, T.E., Haberland, M., Reddy, T., Cournapeau, D., Burovski, E., Peterson, P., Weckesser, W., Bright, J., van der Walt, S.J., Brett, M., Wilson, J., Millman, K.J., Mayorov, N., Nelson, A.R.J., Jones, E., Kern, R., Larson, E., Vázquez-Baeza, Y., 2020. SciPy 1.0: fundamental algorithms for scientific computing in Python. Nat. Methods 17 (3), 261–272. https://doi.org/10.1038/s41592-019-0686-2.

Vogel, H., Gerke, H.H., Mietrach, R., Zahl, R., Wöhling, T., 2023. Soil hydraulic conductivity in the state of nonequilibrium. Vadose Zone J. 22 (2), e20238. https://doi.org/10.1002/vzj2.20238.

Wersäll, C., Nordfelt, I., Larsson, S., 2016. Soil compaction by vibratory roller with variable frequency. Geotechnique 67, 272–278. https://doi.org/10.1680/jgeot.16.P.051.

Yadav, G.S., Lal, R., Meena, R.S., 2020. Vehicular traffic effects on hydraulic properties of a Crosby silt loam under a long-term no-till farming in Central Ohio, USA. Soil Tillage Res. 202. https://doi.org/10.1016/j.still.2020.104654.

Zhang, B., Jia, Y., Fan, H., Guo, C., Fu, J., Li, S., Li, M., Liu, B., Ma, R., 2024. Soil compaction due to agricultural machinery impact: a systematic review. Land Degrad. Dev. 35 (10), 3256–3273. https://doi.org/10.1002/ldr.5144.